HHS Public Access

Author manuscript

Nat Photonics. Author manuscript; available in PMC 2023 August 01.

Published in final edited form as:

Nat Photonics. 2023 February ; 17(2): 179–186. doi:10.1038/s41566-022-01116-6.

Six-Dimensional Single-Molecule Imaging with Isotropic Resolution using a Multi-View Reflector Microscope

Oumeng Zhang[1], **Zijian Guo**[2], **Yuanyuan He**[2], **Tingting Wu**[1], **Michael D. Vahey**[2,3], **Matthew D. Lew**[1,3,4,*]

[1]Department of Electrical and Systems Engineering.

[2]Department of Biomedical Engineering.

[3]Center for Biomolecular Condensates.

[4]Institute of Materials Science and Engineering, Washington University in St. Louis, Missouri 63130, USA.

Abstract

Imaging both the positions and orientations of single fluorophores, termed single-molecule orientation-localisation microscopy, is a powerful tool to study biochemical processes. However, the limited photon budget associated with single-molecule fluorescence makes high-dimensional imaging with isotropic, nanoscale spatial resolution a formidable challenge. Here, we realise a radially and azimuthally polarized multi-view reflector (raMVR) microscope for the imaging of the 3D positions and 3D orientations of single molecules, with precision of 10.9 nm and 2.0° over a 1.5 μm depth range. The raMVR microscope achieves 6D super-resolution imaging of Nile red (NR) molecules transiently bound to lipid-coated spheres, accurately resolving their spherical morphology despite refractive-index mismatch. By observing the rotational dynamics of NR, raMVR images also resolve the infiltration of lipid membranes by amyloid-beta oligomers without covalent labelling. Finally, we demonstrate 6D imaging of cell membranes, where the orientations of specific fluorophores reveal heterogeneity in membrane fluidity. With its nearly isotropic 3D spatial resolution and orientation measurement precision, we expect the raMVR microscope to enable 6D imaging of molecular dynamics within biological and chemical systems with exceptional detail.

A hallmark of biological systems is their careful control and regulation of biomolecular interactions at the nanoscale, via mechanical forces [1], lipid membranes [2], and biomolecular condensates [3, 4], to name a few examples. Owing to their sensitivity and versatility [5, 6], single fluorescent molecules and their translational and rotational dynamics have been used to study a variety of biochemical processes, including the

*Corresponding author(s). mdlew@wustl.edu.

Author contributions

O.Z. and M.D.L. designed and built the raMVR imaging system. Z.G., Y.H., and M.D.V. prepared fixed HEK293T cells. T.W. developed the protocol for preparing lipid-coated silica spheres. O.Z. performed experiments and analyzed the data.

Competing interests

A patent application covering the raMVR imaging technology reported in this manuscript has been filed by Washington University (O.Z. and M.D.L. inventors, application number PCT/US2021/063071). The remaining authors declare no competing interests.

motions of molecular motors [7, 8], conformations of supercoiled DNA [9-11], and the structure and organization of actin filaments [12, 13], amyloid aggregates [14, 15], and lipid membranes [16, 17]. Simultaneously resolving the 3D position, 3D orientation, and rotational diffusion of single fluorophores, termed single-molecule orientation-localization microscopy (SMOLM), requires careful manipulation of the phase and polarization of only hundreds or thousands of photons. Limited by challenging signal-to-background ratios (SBRs) in typical single-molecule (SM) experiments, microscopists have developed various SMOLM techniques to improve measurement performance [18], approaching the theoretical limits under ideal conditions [19-21]. To use precious fluorescence photons more efficiently and maximize signal-to-noise ratios (SNRs), most recently developed techniques create dipole-spread functions (DSFs), or images of dipole emitters, with compact footprints [11, 12, 15, 17, 22] and thusly achieve higher precision and accuracy. One key challenge with these designs is that orientation estimation requires fitting subtle features within noisy images. Therefore, optical aberrations must be carefully calibrated, often requiring online measurement of specific sample-induced aberrations [23, 24]. In contrast, orientation-sensitive DSFs based on pupil splitting [25-27] are generally more robust against aberrations because their orientation information is encoded in the relative brightness of well-separated "spots." However, this robustness comes at the cost of typically lower SBRs and worse estimation performance [28].

Here, we present a combined polarization modulation and pupil-splitting technique, termed the radially and azimuthally polarized multi-view reflector (raMVR) microscope, that achieves isotropic imaging resolution and ~1.5 × better precision for measuring 6D SM positions and orientations compared to state-of-the-art techniques while showing excellent robustness against aberrations. We use the raMVR microscope to study model lipid membranes and how amyloid-beta aggregates intercalate within and perturb their structures. We also visualize SM rotational dynamics to reveal heterogeneities in the fluidity of cellular membranes. These data establish the power of raMVR for resolving both the structure and organization of biological targets accurately and precisely with nanoscale resolution.

Results

Operating principle and theoretical performance

Fluorescent molecules are well-approximated as oscillating dipole emitters [29] (Figure 1b), and we model their rotational diffusion as uniform within a hard-edged cone using an orientation vector $\boldsymbol{\mu} = [\mu_x, \mu_y, \mu_z] = [\sin\theta\cos\phi, \sin\theta\sin\phi, \cos\theta]$ and solid angle $\Omega \in [0, 2\pi]$. To measure molecular orientation, our raMVR approach takes inspiration from both polarization modulation [12, 17, 30, 31] and pupil-splitting [25, 26] innovations in SM orientation-localization microscopy (SMOLM). First, the polarized radiation pattern of a dipole emitter may be manipulated to measure its orientation [32-34]; here, we use a vortex half waveplate and polarizing beamsplitter (PBS) (Figure 1a) to separate light from emitters oriented parallel to versus perpendicular to the optical axis [17, 30, 35]. Secondly, we wish to maximize orientation-measurement sensitivity while simultaneously maintaining superior SBRs in SM imaging. We therefore split fluorescence photons at the back focal plane (BFP) or pupil of the microscope using a square pyramidal mirror (Figure 1c), called

the glass pyramid. The resulting four reflected “beams” are directed toward a mirror with four reflective surfaces whose shape is a pyramid hollowed out of a square prism, termed the air pyramid. The apex angle of the air pyramid is slightly smaller compared to that of the glass pyramid (by 1 degree in our system, see Supplementary Section 1) and reflects the fluorescence back in its original direction to create four imaging channels on a camera (Figure 1d). Critically, both signal and background photons are separated across the four channels, thereby maintaining an effective SBR that is similar to a standard unpolarized epifluorescence microscope. While the mirror configuration is similar to that of a Cassegrain reflector (Figure 1c), here we mount our piecewise-planar pyramid mirror from the diagonal directions to avoid blocking any fluorescence (see Extended Data Figures 1-3), achieving a photon efficiency close to 100% and superior to that of metasurfaces [30] and spatial light modulators [15, 25-27].

Figure 1e shows raMVR images captured from SMs with various orientations. Each SM orientation and degree of rotational diffusion is clearly distinguishable by the varying brightnesses of the focused DSF in each channel. Moreover, because each imaging channel now samples one fourth of the objective’s total aperture, the DSF in each channel *shifts laterally* as the SM’s axial position changes [Figure 1e(iv,v) and Movie S1]. This unique method of encoding both position and orientation information enables the raMVR microscope to achieve estimation precisions [calculated via Cramér-Rao bound (CRB) [36], see Supplementary Section 2.3] far superior to that of state-of-the-art methods across a 1.5-μm depth range (Figure 2). With a typical SM SBR of 5000 signal photons (for an in-plane SM at the water-glass interface, $z = 0$) and 40 background photons per 66.8 × 66.8 nm^2 pixel collected across all imaging channels of the raMVR microscope, the average precision for estimating the average orientation $\boldsymbol{\mu}$, wobble Ω, lateral x, and axial z positions are 2.04°, 0.23 sr, 10.8 nm, and 12.2 nm, respectively; these numbers are 47.9%, 43.8%, 25.9%, and 55.2% smaller compared to those of CHIDO [12] and 66.4%, 65.6%, 42.8%, and 62.0% smaller than those of the vortex DSF [11]. Importantly, raMVR’s precision is superior to those of all other orientation-localization methods (see Figure S8 and Tables S1,S2 for other comparisons), over its entire depth range, regardless of the SM’s position and orientation. Due to the reduced effective numerical aperture (NA) with each imaging channel, raMVR exhibits somewhat reduced lateral localization precision; its localization precision is 3.0 nm and 1.2 nm worse than those of coordinate and height super-resolution imaging with dithering and orientation (CHIDO) and the vortex DSF, respectively. However, because of its compact DSF (Extended Data Figure 4), dim defocused SMs and even certain in-focus SMs are easier to detect using the raMVR microscope than when using CHIDO and the vortex DSF (Supplementary Section 2.2). Notably, our detection and estimation algorithm (Supplementary Section 3) maintains these performance advantages on simulated images, attaining an average localization precision of 24% and orientational precision of 5% greater than the CRB (Table S3).

Experimental validation of 6D precision and accuracy

Silica spheres coated with supported lipid bilayers (SLBs) composed of DPPC (1,2-Dipalmitoyl-sn-glycero-3-phosphocholine) and 40% cholesterol (Figure 3a) have been previously shown [22] to be excellent calibration targets for SMOLM since we are able

to systematically control both the morphology and ordering of the lipids within the SLB. By imaging Nile red (NR, Figure S20) molecules transiently bound within the SLBs (using the PAINT blinking mechanism [37]), we resolve spherical structures with radii as small as 150 nm and as large as 1 μm without scanning the sample (Figure 3b,c). Moreover, we observe NR to be perpendicular to the spheres' surfaces, regardless of the spheres' radii (Figure 3d), thereby matching previous observations [15, 16]; the angles $\theta_{\perp}$ between NR's average orientation $\boldsymbol{\mu}$ and the sphere's surface normal vector $\boldsymbol{r}$ are 12.0°±15.0°, 13.5°±17.6°, and 19.0°±20.4° (median ± std. dev.) for 1000-nm, 350-nm, and 150-nm radius spheres, respectively. We also find that NR molecules are moderately constrained in their rotational diffusion with wobble cone angles Ω of 1.12 ± 0.93 sr, 1.13 ± 0.95 sr, and 1.01 ± 1.01 sr for 1000-nm, 350-nm, and 150-nm spheres, respectively. We note that despite the severe refractive index mismatch between water (n_2 = 1.33) and the silica sphere supporting each bilayer (n_s = 1.45, Figure 3a), the raMVR system can image NR throughout the entire spherical SLB without any shape distortions (Figure 3b,c), which has never before been achieved by other SMOLM techniques.

To quantify localization precision, we isolate cross sections of each sphere along various directions θ_{CS} (Figure 3b and Movie S2) and measure the distance r between the each molecule and the center of the sphere (Figure 3c,e). Because of raMVR's isotropic localization precision (Figure 2c,d), our measured localization precision is uniform across all cross-section angles θ_{CS}. The apparent full-width at half-maximum (FWHM) thicknesses of the SLBs are 76.1 nm for 1000-nm spheres (Movie S2), 42.6 nm for 350-nm spheres, and 51.6 nm for 150-nm spheres (Figure S23). The average distances r as functions of θ_{CS} yield eccentricities of 0.23, 0.28, and 0.20 for the 1000-nm, 350-nm, and 150-nm spheres, respectively (Figure 3e), where the length ratio between short and long axes is 0.96 for an eccentricity of 0.28. Thus, the raMVR microscope accurately reconstructs spherical structures with nanoscale resolution.

6D imaging of amyloid and lipid membrane interactions

Nanoscale interactions between lipid membranes and amyloid aggregates are of tremendous interest for studying the pathogenesis of neurodegerative disease [38, 39], and while atomic force and transmission electron microscopes have provided detailed static snapshots of these structures [40, 41], a 3D imaging technique to resolve the morphology and organization of *individual* peptide-lipid structures is still missing. Here, we use the raMVR system to image aggregates of the 42-residue amyloid-beta peptide (Aβ42), which are a primary signature of Alzheimer's disease [42], intercalated within spherical SLBs (Figure 4). We incubated Aβ42 monomers with lipid-coated 350-nm spheres at 37°C with constant shaking (200 rpm). While NR binds to both lipid membranes and Aβ42 aggregates, the sensitivity of NR's rotational dynamics to its chemical environment [15, 16] enables us to resolve pure SLBs [Figure 4c(i)] from those that have been infiltrated by Aβ42. When in contact with amyloid aggregates on the spheres' surfaces, NR shows larger wobble angles [Figure 4c(ii-iv), Ω = 2.98 ± 1.14 sr in panel (ii), 2.33 ± 1.20 sr in panel (iii), and 2.09 ± 1.15 sr in panel (iv)] compared to those within DPPC SLBs (Figure 3d, Ω = 1.13 ± 0.95 sr). This larger wobble with Aβ42 present is also easily distinguished from that within a 100-nm pure lipid vesicle attached to a sphere [Figure 4b(i), Ω = 1.69 ± 0.93 sr, and Movie S3].

Kolmogorov-Smirnov tests of these wobble distributions return *p*-values much less than 0.01 (see Supplementary Section 5.3 for details), thereby confirming that NR exhibits dramatically different orientational dynamics when in contact with regions of the SLBs infiltrated by amyloid aggregates versus pure lipid membranes.

In the presence of lipids, we observe that Aβ42 is more likely to form oligomers and proto-fibrils than long fibril structures, in agreement with previous studies [43, 44]. For example, a cluster of NR exhibiting small wobble angles [Figure 4c(v)] reveals a small Aβ42 aggregate attached to the sphere near the coverslip in Figure 4b(v). We also observed larger aggregates linking multiple spheres (Figure S28). Across more than 25 spheres from 7 separate aggregation reactions (Figure S26), we observe only one occurrence of significant fibril growth (Figure 4 and Movie S3, day 7*). NR molecules bound to the fibril appear to be parallel to its long axis and more rotationally-fixed [Figure 4c(vi), $\Omega = 0.70 \pm 0.67$ sr] compared to those within the SLBs. This result is consistent with previous work [14, 15] and a control experiment of Aβ42 fibrils aggregated in the absence of lipids (Figure S17). Overall, principal component analysis of NR orientation distributions (Supplementary Section 5.4) indicates that Aβ42 aggregation in the presence of lipid membranes is extremely heterogeneous (Figure S25-S27), and membrane disorder generally becomes more heterogeneous with longer Aβ42 aggregation reactions.

6D imaging of the fluidity of HEK-293T cell membranes

Environmentally sensitive fluorophores have exciting promise as moleculesized sensors for visualizing the nanoscale organization of lipid membranes [16, 45-49]. We demonstrate, for the first time, 6D imaging of cell membrane morphology and fluidity by analyzing fluorescence flashes of merocyanine 540 (MC540, Figure S20) transiently binding to fixed HEK-293T cells (Figure 5, Extended Data Figure 5, Movie S4 and Supplementary Section 4). Here, the raMVR microscope measures 3D SM positions and 3D rotational dynamics within a $23 \times 23 \times 2\ \mu m^3$ volume without scanning the sample or focal plane, obtaining an experimental 3D resolution (using Fourier shell correlation [50, 51]) of 64.1 nm (FWHM) for a vesicle (Figure 5a, yellow box and Figure S30a) and 73.0 nm for a planar membrane (Figure 5a, green box and Figure S30b). First, we examine the rotational mobility of MC540 molecules across various regions of the membrane. We observe smaller MC540 wobble (2.12 ± 1.40 sr, median ± std. dev., Extended Data Figure 5d) near the cell-coverslip interface compared to that for membranes above the coverslip (3.62 ± 1.17 sr, Extended Data Figure 5d), suggesting that the rigidity of the coverglass reduces membrane fluidity and thus constrains the rotational motions of MC540. In contrast, the tip of a membrane protrusion exhibits larger wobble angles (3.83 ± 0.98 sr, Figure 5d) compared to its middle (3.11 ± 1.16 sr, Figure 5d). Previous studies have shown that dye wobble is proportional to the degree of intermolecular spacing and fluidity within the membrane [15, 16, 22], implying that lipids within the protrusion's tip also are more fluid than those in surrounding regions.

Next, we quantify the tilt of MC540 relative to the membrane surface (within the *xy*-plane) as $\Delta\phi = \phi - \phi_{membrane} \in [0°, 180°]$, where $\phi_{membrane}$ is computed using first-order least mean-square error (LMSE) fits of the localizations in regions (i)-(iv) in Figure 5d,e and Extended Data Figure 5d,e. Similar to NR bound to DPPC SLBs (Figure 3), cross-sectional

SMOLM images (Figure 5c and Extended Data Figure 5c) show that MC540 binds perpendicularly to the membrane surface with tilt given by $\Delta\phi$ = 101.1° ± 29.9° in Figure 5d,f(ii) and $\Delta\phi$ = 88.9° ± 22.1° in Extended Data Figure 5e,f(iv). We also detect MC540 molecules binding parallel to the membrane (Extended Data Figure 5c) with a tilt of $\Delta\phi$ = 0.6° ± 23.8° in Figure 5e,f(iii) (see Figure S31 for raw images). NR4A [49], a NR variant with a membrane-targeting moiety (Figure S20), does not exhibit parallel binding behavior (Extended Data Figure 6).

Interestingly, certain areas show both parallel and perpendicularly oriented MC540 [Extended Data Figure 5e,f(iii): 30% parallel ($\Delta\phi$ = 4.6° ± 18.3°) and 70% perpendicular ($\Delta\phi$ = 103.2° ± 18.7°) and Figure 5e,f(iv): 28% parallel ($\Delta\phi$ = 83.6° ± 20.8°) and 72% perpendicular ($\Delta\phi$ = 0.4° ± 17.0°)]. The ratio of parallel to perpendicularly oriented MC540 even varies within a continuous region of the membrane (Extended Data Figure 5d); 37% parallel ($\Delta\phi$ = 6.1° ± 15.1°) vs. 63% perpendicular MC540 ($\Delta\phi$ = 89.7° ± 25.5°) in Extended Data Figure 5d,f(i) morphs into virtually completely perpendicular MC540 in Extended Data Figure 5d,f(ii) ($\Delta\phi$ = 78.0° ± 28.3°). Ensemble experiments have also found MC540 to be aligned both parallel and perpendicular to model membranes [52, 53], but because of its SM sensitivity and nanoscale resolution, raMVR imaging resolves spatial heterogeneities in the fluidity of HEK-293T membranes. The variations in MC540 orientations likely stem from variations in lipid composition, phase, and packing of the membrane [55, 56], charges within the membrane [52], and consequent variations in the concentration of MC540 molecules [54, 57].

Discussion

In summary, we demonstrate the design of a radially and azimuthally polarized multiview reflector (raMVR) microscope for 6D imaging of fluorescent molecules in SMOLM. When imaging Nile red binding to spherical supported lipid bilayers (Figure 3), we observe rotationally-fixed molecules perpendicular to the membrane and achieve a 3D experimental localization precision of ~16.0 nm (std. dev., corresponding to an FWHM of 42.6 nm for 350-nm spheres) with 5000 signal photons detected. We reconstruct nearly perfectly spherical SLBs with radii from 150 nm up to 1 μm, thereby confirming the raMVR system's robustness against refractive index mismatch (Supplementary Section 3.7). We also resolve, for the first time to our knowledge, Aβ42 aggregates intercalating with lipid membranes in 3D with nanoscale resolution (Figure 4). NR molecules bound to mixed oligomer-lipid membranes typically exhibit larger rotational motions compared to those bound to pure lipid membranes, whereas NR bound to fibrils are more fixed and oriented parallel to the long-axis grooves of their stacked β-sheets. Finally, 6D SMOLM of fixed HEK-293T cells (Figure 5 and Extended Data Figure 5) resolves variations in membrane fluidity throughout the cell. Despite the relative complexity of natural cell membranes, we detect MC540 binding both parallel and perpendicular to the membrane, similar to behaviors previously observed on model membranes [52, 53]. Notably, we also observe MC540 molecules that are neither parallel nor perpendicular to the membrane [$\Delta\phi$ = 62.2° ±31.3° in Figure 5d,f(i)]. This observation raises the intriguing possibility that MC540 can be used to interrogate complex molecular interaction networks within biological cell membranes, such as those mediated by the cytoskeleton [13] and membrane proteins [1]. Overall, a distinguishing

characteristic of our Aβ42-lipid membrane and HEK-293T cell membrane 6D imaging is strong nanoscale heterogeneity in both orientational alignments and rotational diffusion exhibited by Nile red and merocyanine 540. Exploring how these behaviors are correlated with peptide identity, membrane composition, and dye structure will be exciting subjects of future studies.

The heart of the raMVR design is the integration of a vortex waveplate and pyramidal mirrors to precisely manipulate and split polarized SM fluorescence into multiple imaging channels. One disadvantage of this design is its alignment complexity; we provide detailed schematics (Extended Data Figures 1-3 and Figure S1) and alignment protocols (Supplementary Section 1) to mitigate these challenges. However, much like telescopes, the reflective geometry has outstanding and unique advantages for nanoscopic imaging of dim light sources; splitting both signal and background into separate channels enables 6D position and orientation measurements with minimal light loss, a large ~2 μm depth range, and a relatively compact DSF. The raMVR mirror is specifically designed to encode molecules' 3D positions into lateral shifts of the DSF [Figure 1e(iv,v)] and their 3D orientations into the relative brightness of the DSF in each channel (Figure S4). Thus, unlike most other methods, position and orientation information are disentangled, and the combined 6D measurement is robust across a range of *in vitro* and cellular targets. This strategy yields isotropic 3D spatial resolution, with raMVR achieving ~26-59% smaller standard deviations on average for measuring the 3D positions and orientations compared to recent, state-of-the-art methods [11-13, 15, 17].

We believe the raMVR pupil-splitting approach has many exciting possibilities for further development. It can be adapted for real-time orientation-resolved epifluorescence microscopy (Figure S17) of cellular structures. Since the 3D information within raMVR images is encoded similarly to that of SM light-field microscopy [58], utilizing a fast 3D deconvolution algorithm should enable high-throughput polarization-resolved 3D imaging with larger FOVs and higher temporal resolution than demonstrated here. In addition, light-sheet illumination [59, 60] should reduce background autofluorescence for extended-depth imaging. Finally, rapid advancements in deep learning for SM microscopy [61-64] could enable real-time 6D SMOLM imaging of cells and tissues, shedding light on a variety of cellular processes with unprecedented detail.

Methods

Imaging system

A 100×, 1.5 NA total internal reflection fluorescence (TIRF) objective lens (OL, Olympus UPLAPO100XOHR) and an achromatic tube lens (TL, f = 175 mm) create an intermediate image plane (IIP). Two 4f systems (L1, L2 and L3-L5, f_{4f} = 150 mm) then project the intermediate image planes to the cameras and create conjugate pupil planes for the waveplates and MVR mirrors of the system. A variable waveplate (VaWP, Thorlabs LCC1223-A, Figure 1a) and a vortex half waveplate (VWP, Thorlabs WPV10L-633, Figure 1a) are placed before and at the back focal plane (BFP), respectively, in the first 4f system (L1, L2). They convert radially and azimuthally polarized light to x- and y-polarized light, compensating for the birefringence of the dichroic mirrors used in our experiments

[17, 30] and are calibrated and aligned according to the procedure reported previously [17]. A polarizing beamsplitter (PBS, Meadowlark Optics BB-100-VIS) is placed in the second 4f system (L3-L5, Extended Data Figure 3a) to create separate imaging channels containing radially or azimuthally polarized fluorescence collected from the sample. After being separated by the MVR mirrors, the polarized fluorescence is captured by detectors C1 (Hamamatsu ORCA-flash4.0v2 C11440-22CU) and C2 (Hamamatsu ORCA-flash4.0v3 C13440-20CU); the effective pixel size is 66.8 × 66.8 nm^2 in object space. The detailed dimensions and placement of the pyramid mirrors are documented in Supplementary Section 1.

Forward imaging model

For a molecule located at position $\boldsymbol{r} = [x, y, z]^\top$ with orientational second moments $\boldsymbol{m} = [m_{xx}, m_{yy}, m_{zz}, m_{xy}, m_{xz}, m_{yz}]^\top$, the image $I(u, v)$ formed by a microscope is given by

$$\begin{aligned} \boldsymbol{I}(u,v) &= s\boldsymbol{B}\boldsymbol{m} + b(u,v) \\ &= s\big[B_{xx}(u,v;\boldsymbol{r})m_{xx} + B_{yy}(u,v;\boldsymbol{r})m_{yy} \\ &\quad + B_{zz}(u,v;\boldsymbol{r})m_{zz} + B_{xy}(u,v;\boldsymbol{r})m_{xy} \\ &\quad + B_{xz}(u,v;\boldsymbol{r})m_{xz} + B_{yz}(u,v;\boldsymbol{r})m_{yz}\big] \\ &\quad + b(u,v) \end{aligned} \tag{1}$$

where (u, v) represents the image plane coordinate system, s represents the number of signal photons, $b(u, v)$ represents the background fluorescence from the sample, and $B_{ij}(u, v; \boldsymbol{r})$ are termed the basis images (Figure S4) of the imaging system that depend on the position of the molecule (see Supplementary Section 2.1 for details). We note that the BFP segmentation guarantees that the basis images in the image plane are linearly independent with respect to the six second moments (Figure S4). The DSF in each channel translates along the x direction as an emitter translates in the x direction, as shown by the spatial gradient of each basis image [Figure S5(i-iii)]. However, if an emitter translates axially, each channel shifts laterally in a unique direction [Figure S5(iv-vi)], thereby enabling 3D positions to be estimated from the lateral positions of corresponding DSFs across all 8 channels. We also note that the direction of the k-vector of each channel is tilted by 1° relative to the camera normal. Thus, the apparent lateral shift caused by the non-normal propagation vector is negligible compared to that caused by the partitioning of the BFP.

Detection and estimation algorithms for raMVR imaging

To localize SMs within MVR images for single-molecule orientation-localization microscopy (SMOLM), we need to group the DSFs detected across the 8 imaging channels to their corresponding molecules, i.e., assign spots detected in each channel to unique (x, y, z) positions corresponding to each emitter. Further, depending on the orientation of a particular emitter, one or more channels will contain no or very few photons, e.g., channels 6 and 8 for a molecule with orientation ($\theta = 90°$, $\phi = 0°$, Ω = 0 sr) [Figure 1e(i)] or channels 2 and 4 for a molecule with orientation ($\theta = 90°$, $\phi = 45°$, Ω = 0 sr) [Figure 1e(ii)]. While these “empty” channels improve the raMVR system’s orientation sensitivity, because these channels are only dark for specific orientations, this phenomenon makes spot assignment more challenging.

Briefly, detecting and localizing SMs follows a three-step process. First, a regularized maximum likelihood estimator is used to detect and localize SMs independently in each imaging channel (Supporting Section 3.2). Next, the coarse 3D position of each SM is calculated by grouping DSF images together across imaging channels. Finally, the 3D position and 3D orientation of each SM is estimated using maximum likelihood estimation (Supporting Section 3.3). This approach yields excellent estimation precision and accuracy (Table S3).

Sample preparation

Lipid-coated silica spheres—We follow previously reported procedures [16, 17, 22] for preparing lipid-coated silica spheres. First, we prepare large unilamellar vesicles (LUVs) composed of DPPC and 40% cholesterol. A mixture of 17.62 μL of the stock DPPC solution (25 mg/mL DPPC in chloroform, Avanti Polar Lipids 850355C) and 15.46 μL of 10 mg/mL cholesterol (Sigma-Aldrich C8667) in chloroform are placed under vacuum overnight to evaporate the chloroform. The dried lipid mixture is then resuspended in 1 mL Tris Ca^{2+} buffer (100 mM NaCl, 3 mM Ca^{2+}, 10 mM Tris, pH 7.4) to arrive at a lipid concentration of 1 mM. The lipid solution is kept under nitrogen in a water bath at 65 °C and vortexed for 20 seconds every 5 minutes for a total of 6 repetitions. The solution is then moved to an extruder set (Avanti Polar Lipids 610000) kept on a hot plate to maintain its temperature above the phase transition temperature of DPPC. A 25-passage extrusion is performed to improve the homogeneity of the size distribution of the final suspension.

We next dilute silica spheres (Bangs Laboratories SS02001, SS03001, SS04002, 2 g/mL) using Tris Ca^{2+} to reach a concentration of 40 μg/mL. It is further diluted in Tris Ca^{2+} according to Table S4. The diluted sphere solution is warmed by immersing it in a 65° C water bath and then mixed with the lipid LUV solution. The volume of each component (Table S4) ensures full coverage of SLBs on the surfaces of the spheres [65]. The mixture is kept in the water bath for 30 minutes and then gradually cooled to room temperature. We vortex the mixture every 5 minutes during the entire process. Finally, we centrifuge the mixture at a speed according to the sphere size (Table S4) and replace the Tris Ca^{2+} supernatant with Tris (for DPPC SLB imaging, 100 mM NaCl, 10 mM Tris, pH 7.4) or PBS (for SLBs mixed with Aβ42 imaging, 100 mM NaCl, 50 mM Na_2PO_4, pH 7.4).

Amyloid-beta 42 aggregation—The Aβ42 sample is prepared according to previously reported procedures [14, 15]. To image the interaction between model lipid and amyloid, we incubate 20 μM monomeric Aβ42 and 1 μg/mL lipid-coated 350-nm spheres at 37 °C with 200 rpm shaking. For imaging Aβ42 fibrils on coverglass, only 10 μM monomeric Aβ42 is incubated for 48 hours.

HEK-293T cell culture—HEK-293T cells (ATCC CRL-3216) are maintained in Dulbecco's modified eagle medium (DMEM, Thermo Fisher 10569044) supplemented with 10% fetal bovine serum (Thermo Fisher 26140079) and 1X Antibiotic-Antimycotic Solution (Corning 30004CI). To prepare fixed cell sample, we plate HEK-293T cells at 50% confluency on 8-chamber coverglass (Cellvis C8-1.5H-N) treated with fibronectin (Sigma-Aldrich FC010), according to the manufacturer's protocol. The cells are returned to

the incubator for 24 hours before they are fixed on ice with 2% paraformaldehyde in PBS for 20 minutes.

Extended Data

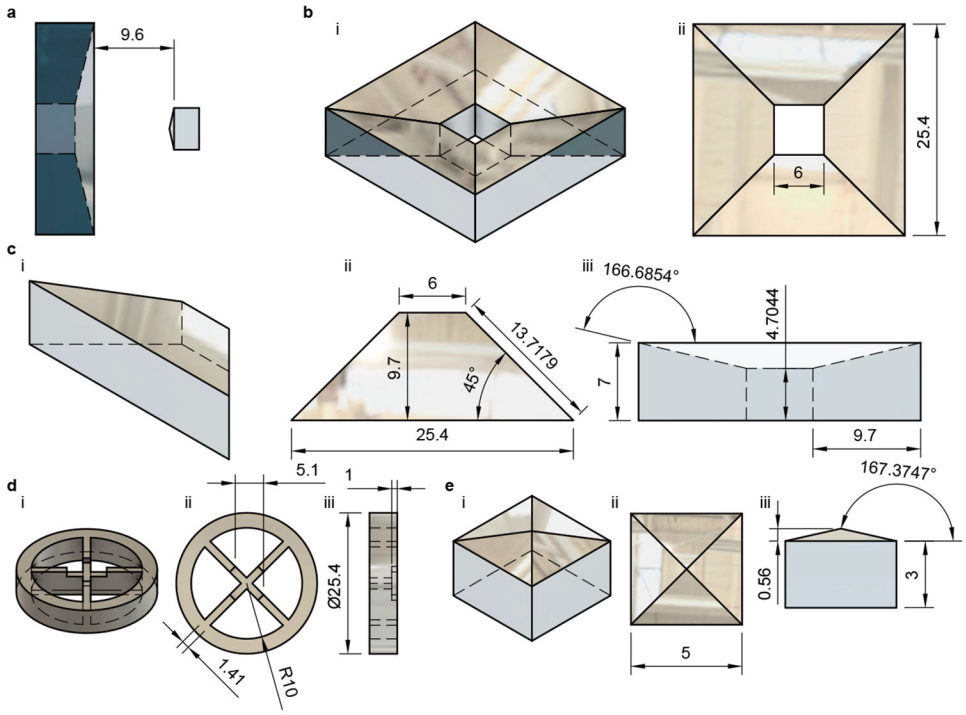

Extended Data Figure 1.

Pyramid mirror designs. (a) Alignment of the pyramidal mirrors and (b-e) dimensions of the (b) air pyramid, (c) one sector of the air pyramid, (d) mount for glass pyramid, and (e) glass pyramid. (i) Isometric view, (ii) top view, and (iii) side view of the mirrors and mount. Length unit: mm.

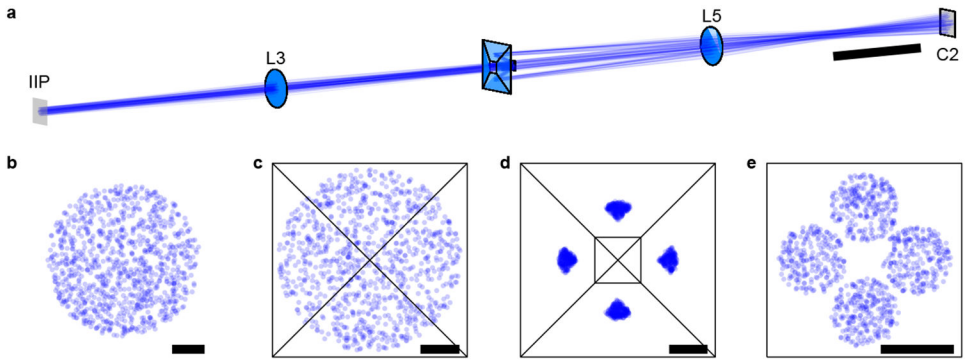

Extended Data Figure 2.

Simulation of rays propagating in the MVR system. A total of 100 rays, randomly oriented within the imaging system's numerical aperture and originating from random positions within the IIP are shown. (a) Three-dimensional view of rays propagating within one of the

polarized imaging channels. (b-d) Position of each ray at the (b) IIP, (c) glass pyramid, (d) air pyramid, and (e) detector. Scale bars: 50 mm in (a), 1 mm in (b,c), 5 mm in (d,e).

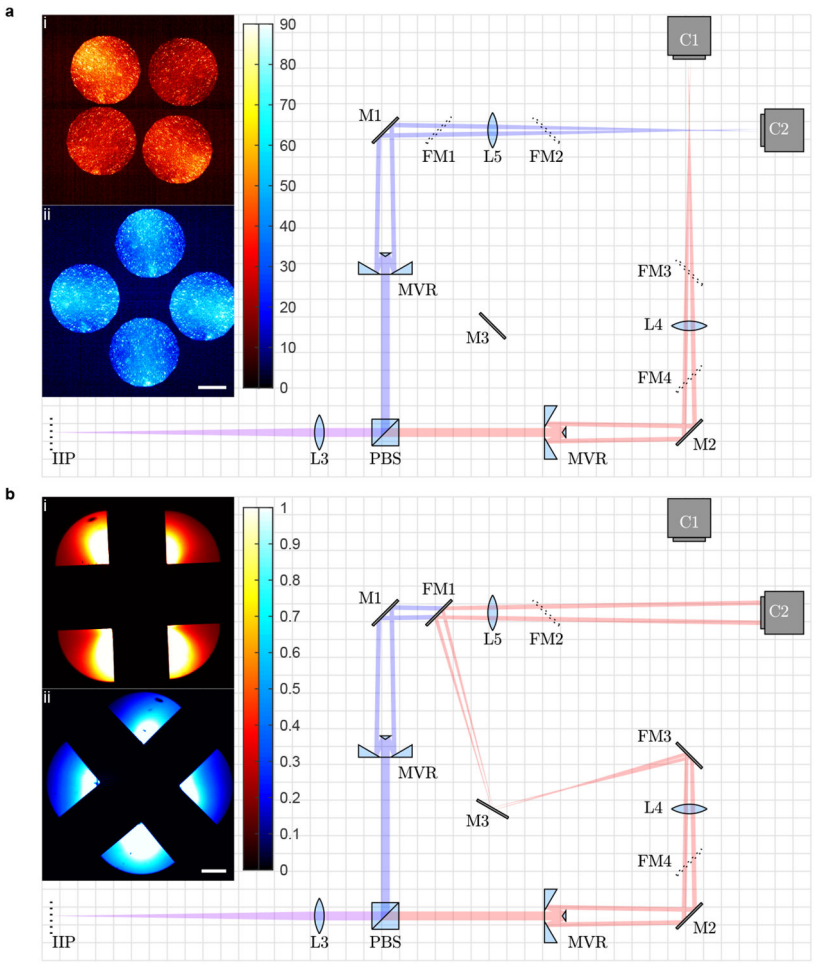

Extended Data Figure 3.

Light propagation within the second 4f system of the raMVR microscope. (a) When folding mirrors FM1-4 are out of the emission path, detectors C1 and C2 observe the (i) radially and (ii) azimuthally polarized image plane. Colourbar: photons; scale bar: 2 μm. (b) When FM1 and FM3 are in the emission path and mirror M3 is properly aligned, detector C2 captures the (i) radially polarized BFP. Similarly, when FM2 and FM4 are in the emission path, detector C1 captures the (ii) azimuthally polarized BFP. Grid size: 1 cm; colourbar: normalized intensity; scale bar: 1 mm.

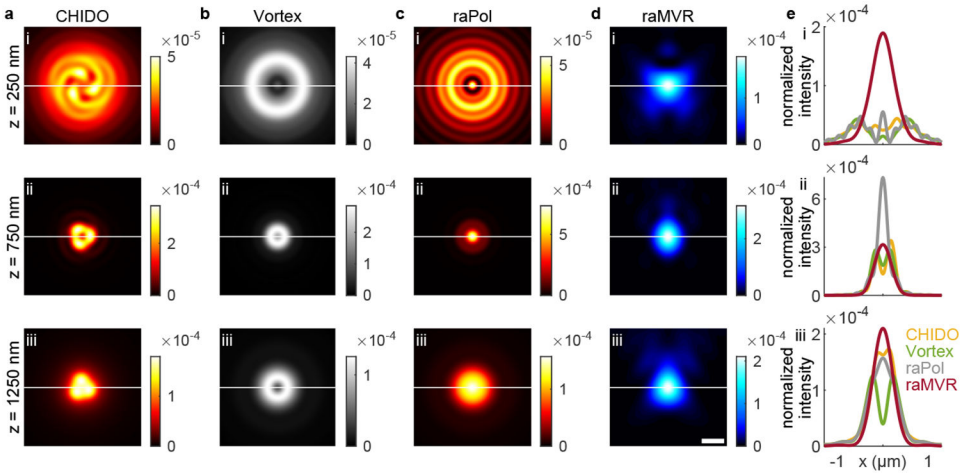

Extended Data Figure 4.

Image size comparison of CHIDO, the vortex DSF, raPol standard DSF and raMVR. (a-d) Images and (e) line profiles of (a) CHIDO (*x*-polarized channel), (b) the Vortex DSF, (c) raPol standard DSF (radially polarized channel), and (d) raMVR (azimuthally polarized channel) for isotropic emitters located at $z = 250$ nm, $z = 750$ nm (best focus), and $z = 1250$ nm. The nominal focal plane $z_f = 1200$ nm. Colourbar: normalized intensity; scale bar: 500 nm. (e) Line profiles of the DSFs in (a-d). Yellow: CHIDO; green: Vortex DSF; gray: raPol standard DSF; red: raMVR.

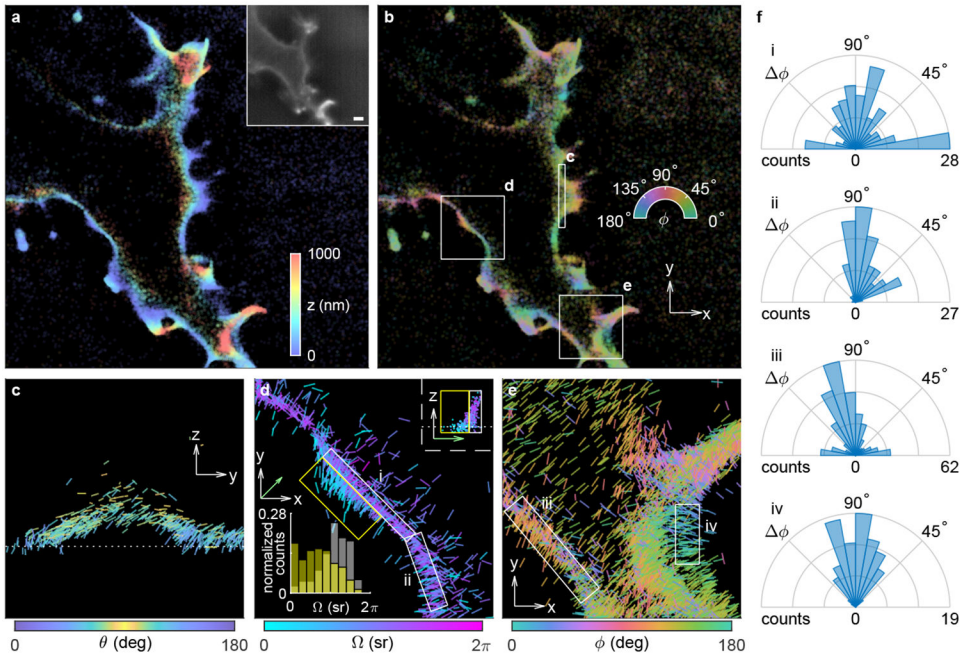

Extended Data Figure 5.

6D nanoscopic imaging of MC540 molecules bound to the membranes of another HEK-293T cell. (a,b) Super-resolved images of two representative cells. Colours represent the estimated (a) axial position *z* and (b) azimuthal angle ϕ. Inset: summed diffraction-limited images from all imaging channels captured under lower excitation power. Scale bar:

2 μm. (c) *yz*- and (d,e) *xy*-views of boxed regions in (b). Lines are oriented and colour-coded according to the measured (c) polar angle θ, (d) wobble angle Ω, and (e) azimuthal angle ϕ. Their lengths are proportional to (c) $\sqrt{\mu_y^2 + \mu_z^2}$ and (d,e) sin θ. Scale arrows: 2 μm in (a,b), 500 nm in (c-e). (d) Insets show the distribution of measured wobble angle Ω within the yellow and white boxed areas (i,ii) and a side view of yellow and white boxed areas (i). Three-dimensional animations of the localizations in (c-e) are shown in Movie S5. (f) MC540 tilt $\Delta\phi$ relative to the membrane surface within the white boxed areas in (d,e).

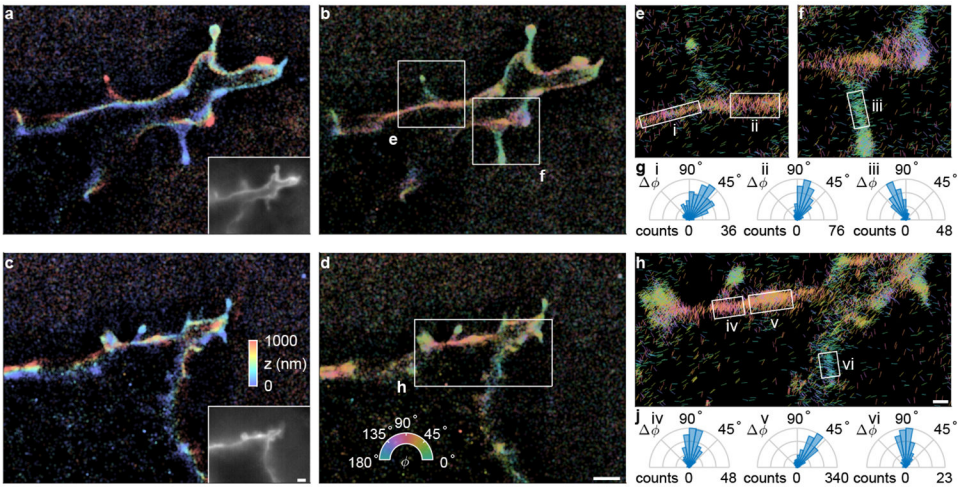

Extended Data Figure 6.

6D nanoscopic imaging of NR4A molecules bound to the membranes of HEK-293T cells. (a-d) Super-resolved images of two representative cells. Colours represent the estimated (a,c) axial position *z* and (b,d) azimuthal angle ϕ. Insets: summed diffraction-limited images from all imaging channels captured under lower excitation power. Scale bar: 2 μm. (e,f,h) The zoomed regions of interest in (b,d). Lines are oriented and colour-coded according to the measured azimuthal angle ϕ. Their lengths are proportional to sin θ. Scale bar: 500 nm. (g, j) Distributions of measured azimuthal angle from the membrane $\Delta\phi$ within the white boxed areas in (e,f,h).

Supplementary Material

Refer to Web version on PubMed Central for supplementary material.

Acknowledgements

We thank Dr. Adam Backer and Dr. Victor Acosta for helpful discussions in designing the raMVR microscope. Amyloid-beta 42 peptide was synthesized and purified by Dr. James I. Elliott (ERI Amyloid Laboratory, Oxford, CT). Research reported in this publication was supported by the National Institute of Allergy and Infectious Diseases under grant number R21AI163985 to M.D.V., by the National Science Foundation under grant number ECCS-1653777 to M.D.L., and by the National Institute of General Medical Sciences of the National Institutes of Health under grant number R35GM124858 to M.D.L.

Data availability

The data underlying this study are openly available from OSF at https://osf.io/s8m4x/ and by request.

Code availability

The code used to analyze the data is available at https://osf.io/s8m4x/.

References

[1]. Norregaard K, Metzler R, Ritter CM, Berg-Sørensen K & Oddershede LB Manipulation and Motion of Organelles and Single Molecules in Living Cells. Chemical Reviews 117 (5), 4342–4375 (2017). 10.1021/acs.chemrev.6b00638 . [PubMed: 28156096]

[2]. Stone MB, Shelby SA & Veatch SL Super-Resolution Microscopy: Shedding Light on the Cellular Plasma Membrane. Chemical Reviews 117 (11), 7457–7477 (2017). 10.1021/acs.chemrev.6b00716 . [PubMed: 28211677]

[3]. Lyon AS, Peeples WB & Rosen MK A framework for understanding the functions of biomolecular condensates across scales. Nature Reviews Molecular Cell Biology 22 (3), 215–235 (2021). 10.1038/s41580-020-00303-z . [PubMed: 33169001]

[4]. Emenecker RJ, Holehouse AS & Strader LC Biological Phase Separation and Biomolecular Condensates in Plants. Annual Review of Plant Biology 72 (1), 17–46 (2021). 10.1146/annurev-arplant-081720-015238 .

[5]. Moerner WE & Kador L Optical detection and spectroscopy of single molecules in a solid. Physical Review Letters 62 (21), 2535–2538 (1989). 10.1103/PhysRevLett.62.2535 . [PubMed: 10040013]

[6]. Moerner WE Viewpoint: Single Molecules at 31: What's Next? Nano Letters 20 (12), 8427–8429 (2020). 10.1021/acs.nanolett.0c04042 . [PubMed: 33170016]

[7]. Asenjo AB, Krohn N & Sosa H Configuration of the two kinesin motor domains during ATP hydrolysis. Nature Structural & Molecular Biology 10 (10), 836–842 (2003). 10.1038/nsb984 .

[8]. Beausang JF, Shroder DY, Nelson PC & Goldman YE Tilting and Wobble of Myosin V by High-Speed Single-Molecule Polarized Fluorescence Microscopy. Biophysical Journal 104 (6), 1263–1273 (2013). 10.1016/j.bpj.2013.01.057 . [PubMed: 23528086]

[9]. Backer AS, Lee MY & Moerner WE Enhanced DNA imaging using super-resolution microscopy and simultaneous single-molecule orientation measurements. Optica 3 (6), 659 (2016). 10.1364/OPTICA.3.000659 .

[10]. Backer AS et al. Single-molecule polarization microscopy of DNA inter-calators sheds light on the structure of S-DNA. Science Advances 5 (3) (2019). 10.1126/sciadv.aav1083 .

[11]. Hulleman CN et al. Simultaneous orientation and 3D localization microscopy with a Vortex point spread function. Nature Communications 12 (1), 5934 (2021). 10.1038/s41467-021-26228-5 .

[12]. Curcio V, Alemán-Castañeda LA, Brown TG, Brasselet S & Alonso MA Birefringent Fourier filtering for single molecule coordinate and height super-resolution imaging with dithering and orientation. Nature Communications 11 (1), 5307 (2020). 10.1038/s41467-020-19064-6 .

[13]. Rimoli CV, Valades-Cruz CA, Curcio V, Mavrakis M & Brasselet S 4polar-STORM polarized super-resolution imaging of actin filament organization in cells. Nature Communications 13 (1), 301 (2022). 10.1038/s41467-022-27966-w .

[14]. Ding T, Wu T, Mazidi H, Zhang O & Lew MD Single-molecule orientation localization microscopy for resolving structural heterogeneities between amyloid fibrils. Optica 7 (6), 602 (2020). 10.1364/OPTICA.388157 . [PubMed: 32832582]

[15]. Ding T & Lew MD Single-Molecule Localization Microscopy of 3D Orientation and Anisotropic Wobble Using a Polarized Vortex Point Spread Function. The Journal of Physical Chemistry B 125 (46), 12718–12729 (2021). 10.1021/acs.jpcb.1c08073 . [PubMed: 34766758]

[16]. Lu J, Mazidi H, Ding T, Zhang O & Lew MD Single-Molecule 3D Orientation Imaging Reveals Nanoscale Compositional Heterogeneity in Lipid Membranes. Angewandte Chemie International Edition 59 (40), 17572–17579 (2020). 10.1002/anie.202006207 . [PubMed: 32648275]

[17]. Zhang O, Zhou W, Lu J, Wu T & Lew MD Resolving the Three-Dimensional Rotational and Translational Dynamics of Single Molecules Using Radially and Azimuthally Polarized Fluorescence. Nano Letters 22 (3), 1024–1031 (2022). 10.1021/acs.nanolett.1c03948 . [PubMed: 35073487]

[18]. Backlund MP, Lew MD, Backer AS, Sahl SJ & Moerner WE The Role of Molecular Dipole Orientation in Single-Molecule Fluorescence Microscopy and Implications for Super-Resolution Imaging. ChemPhysChem 15 (4), 587–599 (2014). 10.1002/cphc.201300880 . [PubMed: 24382708]

[19]. Zhang O & Lew MD Quantum limits for precisely estimating the orientation and wobble of dipole emitters. Physical Review Research 2 (3), 033114 (2020). 10.1103/PhysRevResearch.2.033114 . [PubMed: 32832916]

[20]. Zhang O & Lew MD Single-molecule orientation localization microscopy II: a performance comparison. Journal of the Optical Society of America A 38 (2), 288 (2021). 10.1364/JOSAA.411983 .

[21]. Beckwith JS & Yang H Information bounds in determining the 3D orientation of a single emitter or scatterer using point-detector-based division-of-amplitude polarimetry. The Journal of Chemical Physics 155 (14), 144110 (2021). 10.1063/5.0065034 . [PubMed: 34654316]

[22]. Wu T, Lu J & Lew MD Dipole-spread-function engineering for simultaneously measuring the 3D orientations and 3D positions of fluorescent molecules. Optica 9 (5), 505 (2022). 10.1364/OPTICA.451899 . [PubMed: 35601691]

[23]. Mlodzianoski MJ et al. Active PSF shaping and adaptive optics enable volumetric localization microscopy through brain sections. Nature Methods 15 (8), 583–586 (2018). 10.1038/s41592-018-0053-8 . [PubMed: 30013047]

[24]. Xu F et al. Three-dimensional nanoscopy of whole cells and tissues with in situ point spread function retrieval. Nature Methods 17 (5), 531–540 (2020). 10.1038/s41592-020-0816-x . [PubMed: 32371980]

[25]. Backer AS, Backlund MP, Lew MD & Moerner WE Single-molecule orientation measurements with a quadrated pupil. Optics Letters 38 (9), 1521 (2013). 10.1364/OL.38.001521 . [PubMed: 23632538]

[26]. Backer AS, Backlund MP, von Diezmann AR, Sahl SJ & Moerner WE A bisected pupil for studying single-molecule orientational dynamics and its application to three-dimensional super-resolution microscopy. Applied Physics Letters 104 (19), 193701 (2014). 10.1063/1.4876440 . [PubMed: 24926098]

[27]. Zhang O, Lu J, Ding T & Lew MD Imaging the three-dimensional orientation and rotational mobility of fluorescent emitters using the Trispot point spread function. Applied Physics Letters 113 (3), 031103 (2018). 10.1063/1.5031759 . [PubMed: 30057423]

[28]. Zhang O & Lew MD Single-molecule orientation localization microscopy I: fundamental limits. Journal of the Optical Society of America A 38 (2), 277 (2021). 10.1364/JOSAA.411981 .

[29]. Novotny L & Hecht B Principles of Nano-Optics (Cambridge University Press, Cambridge, England, 2012).

[30]. Backlund MP et al. Removing orientation-induced localization biases in single-molecule microscopy using a broadband metasurface mask. Nature Photonics 10 (7), 459–462 (2016). 10.1038/nphoton.2016.93 . [PubMed: 27574529]

[31]. Thorsen RØ, Hulleman CN, Rieger B & Stallinga S Photon efficient orientation estimation using polarization modulation in single-molecule localization microscopy. Biomedical Optics Express 13 (5), 2835 (2022). 10.1364/BOE.452159 . [PubMed: 35774337]

[32]. Böhmer M & Enderlein J Orientation imaging of single molecules by wide-field epifluorescence microscopy. Journal of the Optical Society of America B 20 (3), 554 (2003). 10.1364/JOSAB.20.000554 .

[33]. Lieb MA, Zavislan JM & Novotny L Single-molecule orientations determined by direct emission pattern imaging. Journal of the Optical Society of America B 21 (6), 1210 (2004). 10.1364/JOSAB.21.001210 .

[34]. Axelrod D Fluorescence excitation and imaging of single molecules near dielectric-coated and bare surfaces: a theoretical study. Journal of Microscopy 247 (2), 147–160 (2012). 10.1111/j.1365-2818.2012.03625.x . [PubMed: 22612666]

[35]. Lew MD & Moerner WE Azimuthal Polarization Filtering for Accurate, Precise, and Robust Single-Molecule Localization Microscopy. Nano Letters 14 (11), 6407–6413 (2014). 10.1021/nl502914k . [PubMed: 25272093]

[36]. Moon TK & Stirling WC Mathematical Methods and Algorithms for Signal Processing (Prentice Hall, New Jersey, 2000).

[37]. Sharonov A & Hochstrasser RM Wide-field subdiffraction imaging by accumulated binding of diffusing probes. Proceedings of the National Academy of Sciences 103 (50), 18911–18916 (2006). 10.1073/pnas.0609643104 .

[38]. Haass C & Selkoe DJ Soluble protein oligomers in neurodegeneration: lessons from the Alzheimer's amyloid β-peptide. Nature Reviews Molecular Cell Biology 8 (2), 101–112 (2007). 10.1038/nrm2101 . [PubMed: 17245412]

[39]. Iadanza MG, Jackson MP, Hewitt EW, Ranson NA & Radford SE A new era for understanding amyloid structures and disease. Nature Reviews Molecular Cell Biology 19 (12), 755–773 (2018). 10.1038/s41580-018-0060-8 . [PubMed: 30237470]

[40]. Butterfield SM & Lashuel HA Amyloidogenic Protein-Membrane Interactions: Mechanistic Insight from Model Systems. Angewandte Chemie International Edition 49 (33), 5628–5654 (2010). 10.1002/anie.200906670 . [PubMed: 20623810]

[41]. Bode DC, Freeley M, Nield J, Palma M & Viles JH Amyloid-β oligomers have a profound detergent-like effect on lipid membrane bilayers, imaged by atomic force and electron microscopy. Journal of Biological Chemistry 294 (19), 7566–7572 (2019). 10.1074/jbc.AC118.007195 . [PubMed: 30948512]

[42]. Hampel H et al. Core candidate neurochemical and imaging biomarkers of Alzheimer's disease. Alzheimer's & Dementia 4 (1), 38–48 (2008). 10.1016/j.jalz.2007.08.006 .

[43]. Choucair A, Chakrapani M, Chakravarthy B, Katsaras J & Johnston L Preferential accumulation of Aβ(1-42) on gel phase domains of lipid bilayers: An AFM and fluorescence study. Biochimica et Biophysica Acta (BBA) - Biomembranes 1768 (1), 146–154 (2007). 10.1016/j.bbamem.2006.09.005 . [PubMed: 17052685]

[44]. Hane F, Drolle E, Gaikwad R, Faught E & Leonenko Z Amyloid-β Aggregation on Model Lipid Membranes: An Atomic Force Microscopy Study. Journal of Alzheimer's Disease 26 (3), 485–494 (2011). 10.3233/JAD-2011-102112 .

[45]. Kuo C & Hochstrasser RM Super-resolution Microscopy of Lipid Bilayer Phases. Journal of the American Chemical Society 133 (13), 4664–4667 (2011). 10.1021/ja1099193 . [PubMed: 21405121]

[46]. Moon S et al. Spectrally Resolved, Functional Super-Resolution Microscopy Reveals Nanoscale Compositional Heterogeneity in Live-Cell Membranes. Journal of the American Chemical Society 139 (32), 10944–10947 (2017). 10.1021/jacs.7b03846 . [PubMed: 28774176]

[47]. Klymchenko AS Solvatochromic and Fluorogenic Dyes as Environment-Sensitive Probes: Design and Biological Applications. Accounts of Chemical Research 50 (2), 366–375 (2017). 10.1021/acs.accounts.6b00517 . [PubMed: 28067047]

[48]. Lee S-C et al. Fluorescent Molecular Rotors for Viscosity Sensors. Chemistry - A European Journal 24 (52), 13706–13718 (2018). 10.1002/chem.201801389 . [PubMed: 29700889]

[49]. Danylchuk DI, Moon S, Xu K & Klymchenko AS Switchable Solvatochromic Probes for Live-Cell Super-resolution Imaging of Plasma Membrane Organization. Angewandte Chemie International Edition 58 (42), 14920–14924 (2019). 10.1002/anie.201907690 . [PubMed: 31392763]

[50]. Harauz G & van Heel M Exact filters for general geometry three dimensional reconstruction. Optik. 73 (4), 146–156 (1986) .

[51]. Banterle N, Bui KH, Lemke EA & Beck M Fourier ring correlation as a resolution criterion for super-resolution microscopy. Journal of Structural Biology 183 (3), 363–367 (2013). 10.1016/j.jsb.2013.05.004 . [PubMed: 23684965]

[52]. Dragsten PR & Webb WW Mechanism of the membrane potential sensitivity of the fluorescent membrane probe merocyanine 540. Biochemistry 17 (24), 5228–5240 (1978). 10.1021/bi00617a024 . [PubMed: 728397]

[53]. Verkman AS & Frosch MP Temperature-jump studies of merocyanine 540 relaxation kinetics in lipid bilayer membranes. Biochemistry 24 (25), 7117–7122 (1985). 10.1021/bi00346a015 . [PubMed: 4084566]

[54]. Lagerberg JW, Kallen K-J, Haest CW, VanSteveninck J & Dubbelman TM Factors affecting the amount and the mode of merocyanine 540 binding to the membrane of human erythrocytes. A comparison with the binding to leukemia cells. Biochimica et Biophysica Acta (BBA) - Biomembranes 1235 (2), 428–436 (1995). 10.1016/0005-2736(95)80032-B . [PubMed: 7756353]

[55]. Yu H & Hui S-W Merocyanine 540 as a probe to monitor the molecular packing of phosphatidylcholine: a monolayer epifluorescence microscopy and spectroscopy study. Biochimica et Biophysica Acta (BBA) - Biomembranes 1107 (2), 245–254 (1992). 10.1016/0005-2736(92)90411-E . [PubMed: 1504069]

[56]. Wilson-Ashworth HA et al. Differential Detection of Phospholipid Fluidity, Order, and Spacing by Fluorescence Spectroscopy of Bis-pyrene, Prodan, Nystatin, and Merocyanine 540. Biophysical Journal 91 (11), 4091–4101 (2006). 10.1529/biophysj.106.090860 . [PubMed: 16980369]

[57]. Verkman AS Mechanism and kinetics of merocyanine 540 binding to phospholipid membranes. Biochemistry 26 (13), 4050–4056 (1987). 10.1021/bi00387a046 . [PubMed: 3651436]

[58]. Sims RR et al. Single molecule light field microscopy. Optica 7 (9), 1065 (2020). 10.1364/OPTICA.397172 .

[59]. Gustavsson A-K, Petrov PN & Moerner WE Light sheet approaches for improved precision in 3D localization-based superresolution imaging in mammalian cells [Invited]. Optics Express 26 (10), 13122 (2018). 10.1364/OE.26.013122 . [PubMed: 29801343]

[60]. Ponjavic A, Ye Y, Laue E, Lee SF & Klenerman D Sensitive light-sheet microscopy in multiwell plates using an AFM cantilever. Biomedical Optics Express 9 (12), 5863 (2018). 10.1364/BOE.9.005863 . [PubMed: 31065399]

[61]. Zelger P et al. Three-dimensional localization microscopy using deep learning. Optics Express 26 (25), 33166 (2018). 10.1364/OE.26.033166 . [PubMed: 30645473]

[62]. Möckl L, Roy AR & Moerner WE Deep learning in single-molecule microscopy: fundamentals, caveats, and recent developments [Invited]. Biomedical Optics Express 11 (3), 1633 (2020). 10.1364/BOE.386361 . [PubMed: 32206433]

[63]. Nehme E et al. DeepSTORM3D: dense 3D localization microscopy and PSF design by deep learning. Nature Methods 17 (7), 734–740 (2020). 10.1038/s41592-020-0853-5 . [PubMed: 32541853]

[64]. Nehme E et al. Learning Optimal Wavefront Shaping for Multi-Channel Imaging. IEEE Transactions on Pattern Analysis and Machine Intelligence 43 (7), 2179–2192 (2021). 10.1109/TPAMI.2021.3076873 . [PubMed: 34029185]

[65]. Bayerl T & Bloom M Physical properties of single phospholipid bilayers adsorbed to micro glass beads. A new vesicular model system studied by 2H-nuclear magnetic resonance. Biophysical Journal 58 (2), 357–362 (1990). 10.1016/S0006-3495(90)82382-1 . [PubMed: 2207243]

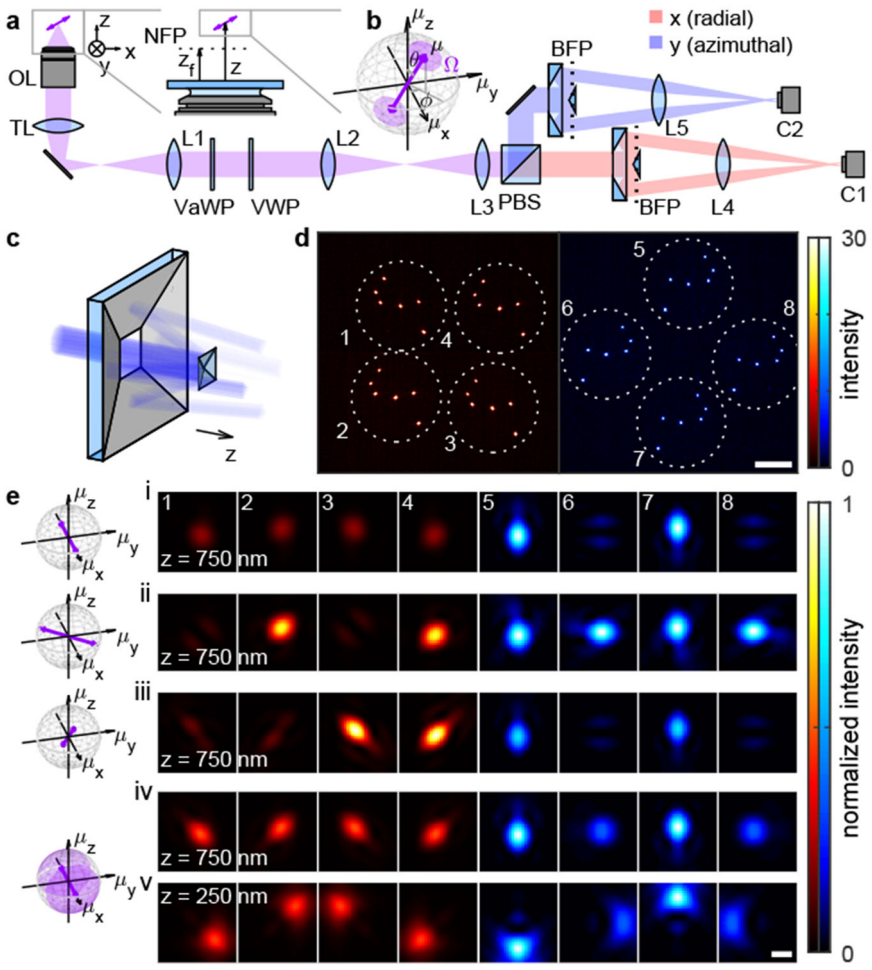

Fig. 1.

Concept of raMVR single-molecule orientation-localization microscopy (SMOLM). (a) Schematic of the radially and azimuthally polarized multi-view reflector (raMVR) microscope. OL: objective lens; TL: tube lens; L1-L5: 4*f* lenses; C1, C2, detectors; NFP, nominal focal plane. (b) The fluorescent molecule is modeled as an oscillating dipole uniformly wobbling within a hard-edged cone with an average orientation $\boldsymbol{\mu}$ and a "wobble" solid angle Ω. After turning radially and azimuthally polarized fluorescence to (red) *x*- and (blue) *y*-polarized light using a variable waveplate (VaWP) and a vortex (half) waveplate (VWP), the emission light is separated into different polarization channels using a polarizing beamsplitter (PBS). The (c) raMVR pyramidal mirrors further separate light at the back focal plane (BFP) into four detection channels and project the (d) image plane onto a detector (C1, C2) in each channel. Dashed lines represent the edge of the field of view. Colourbar: intensity (a.u.); scalebar: 20 μm. (e) Representative dipole spread function (DSF) in each channel for molecules located at (i-iv) $z = 750$ nm and (v) $z = 250$ nm with orientations (θ, ϕ, Ω) of (i) (90°, 0°, 0 sr), (ii) (90°, 45°, 0 sr), (iii) (45°, 0°, 0 sr), and (iv,v) (90°, 0°, π sr). Numbers 1-8 represent the indices of the imaging channels corresponding to those in (d). Colourbar: normalized intensity; scalebar: 500 nm; nominal focal plane position $z_f = 1200$ nm.

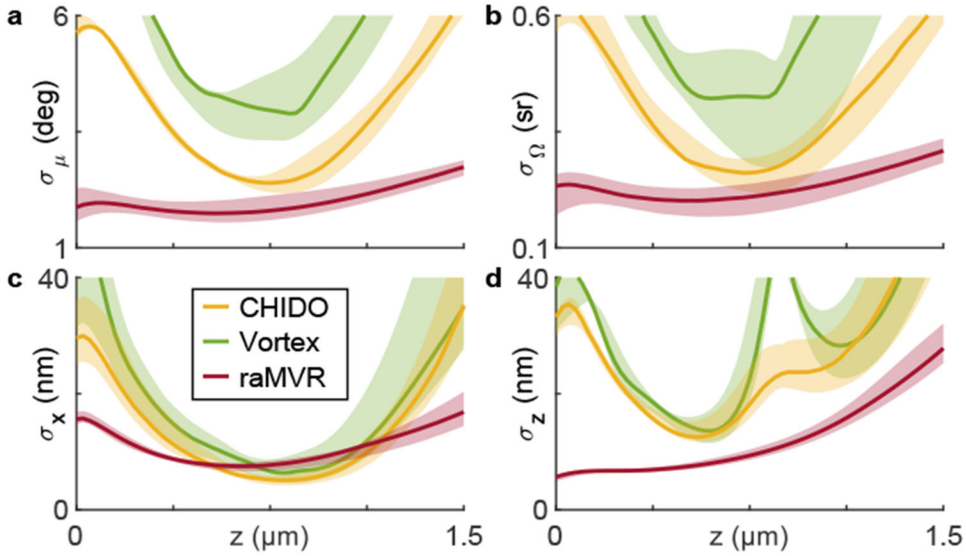

Fig. 2.

Theoretical precision of measuring the (a) average orientation, (b) wobble angle, (c) lateral position, and (d) axial position of an SM using the raMVR microscope compared to other methods, with 5000 signal photons and 40 background photons per pixel total across all channels. Lines represent the median, and shaded areas represent the 10th and 90th percentiles across all possible orientations. Yellow: CHIDO [12]; green: vortex DSF [11]; red: raMVR.

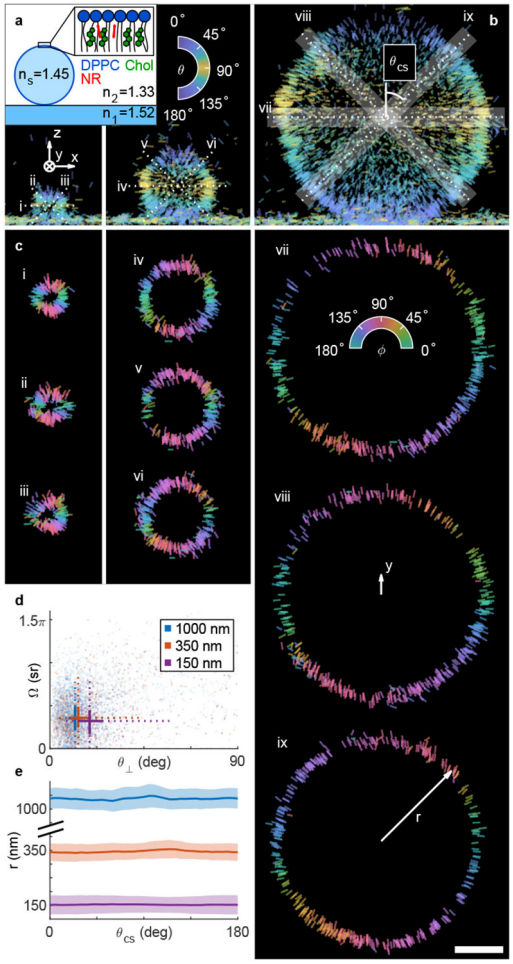

Fig. 3.

6D nanoscopic imaging of spherical supported lipid bilayers (SLBs). (a) Nile red (NR) molecules transiently binding to DPPC SLBs containing 40% cholesterol surrounding a silica sphere. (b) An *xz*-view of all localizations on spheres with radii of 150 nm, 350 nm, and 1000 nm. Lines are oriented and colour-coded according to the measured polar angle θ. Their lengths are proportional to $\sqrt{\mu_x^2 + \mu_z^2}$. (c) Localizations within cross sections with tilt angles θ_{CS} of (i,iv,vii) 90°, (ii,v,viii) −45° and (iii,vi,ix) 45° and thickness of 200 nm. Lines are oriented and colour-coded according to the measured azimuthal angle ϕ. Their lengths are proportional to the length of the unit vector μ projected into the cross-sectional planes. (d) NR orientation $\theta_\perp = \cos^{-1}(\boldsymbol{\mu} \cdot \boldsymbol{r}/r)$ and wobble (Ω) measurements for the three spheres in (b). (e) Measured distances r from NR localizations to the center of the sphere as a function of the cross-section angle θ_{CS}. Solid lines represent the average distance, and shaded areas represent ± 1 std. dev. Blue: 1000-nm spheres; orange: 350-nm spheres; purple: 150-nm spheres. Scalebar: 500 nm.

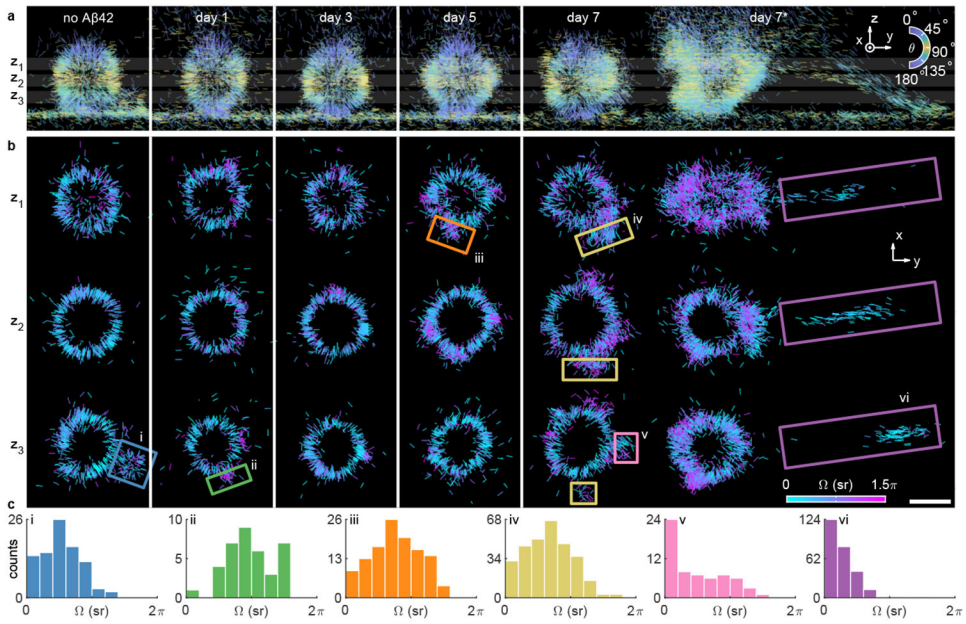

Fig. 4.

6D nanoscopic imaging of amyloid-lipid interaction. (a) *yz*-views of all NR localizations on 350-nm lipid-coated spheres without (incubated for 7 days) and with (incubated for 1, 3, 5, and 7 days) Aβ42. Lines are oriented and colour-coded according to the measured polar angle θ. Their lengths are proportional to $\sqrt{\mu_y^2 + \mu_z^2}$. (b) Localizations within the 150 nm-thick z slices marked in (a) centered at (z_1 = 600, z_2 = 400, z_3 = 200) nm. Lines are oriented according to the measured azimuthal angle ϕ and colour-coded according to the measured wobble cone angle Ω. Their lengths are proportional to sin θ. Scalebar: 500 nm. (c) Distribution of measured wobble cone angles within the boxed areas in (b).

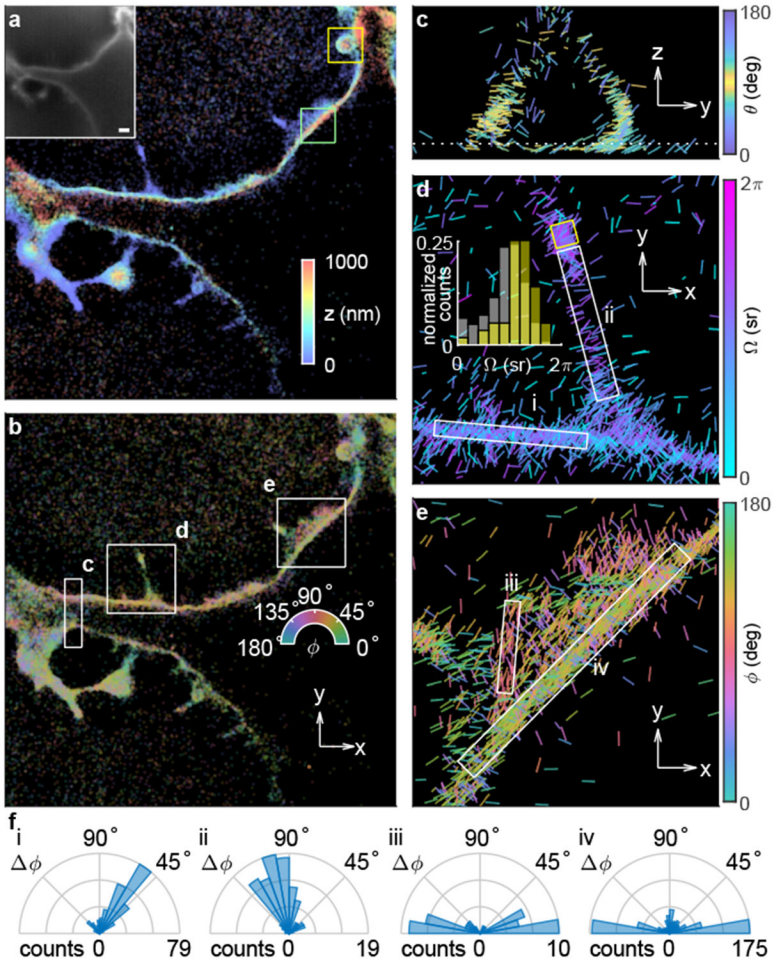

Fig. 5.

6D nanoscopic imaging of MC540 molecules bound to the membranes of an HEK-293T cell. (a-b) Super-resolved images of two representative cells. Colours represent the estimated (a) axial position z and (b) azimuthal angle ϕ. Inset: summed diffraction-limited images from all imaging channels captured under lower excitation power. Scale bar: 2 μm. (c) *yz*- and (d,e) *xy*-views of boxed regions in (b). Lines are oriented and colour-coded according to the measured (c) polar angle θ, (d) wobble angle Ω, and (e) azimuthal angle ϕ. Their lengths are proportional to (c) $\sqrt{\mu_y^2 + \mu_z^2}$ and (d,e) sin θ. Scale arrows: 2 μm in (a-b), 500 nm in (c-e). (d) Insets show the distribution of measured wobble angle Ω within the yellow and white boxed areas (i,ii). Three-dimensional animations of the localizations in (c-e) are shown in Movie S5. (f) MC540 tilt $\Delta\phi$ relative to the membrane surface within the white boxed areas in (d,e).